Hybrid Model Predictive Control Using Reconstructed Voltage Vectors for Postfault Three-Level Voltage Source Inverters

Yong Yang, *Senior Member, IEEE*, Youcheng Wang, Rong Chen, Jiefeng Hu, *Senior Member, IEEE*, Huiqing Wen, *Senior Member, IEEE*, Yiwang Wang, *Member, IEEE*, Hui Yang, *Senior Member, IEEE*, and Jose Rodriguez, *Life Fellow, IEEE*

***Abstract*—Eight-switch three-phase inverters (ESTPIs) offer a promising reconfiguration for addressing single-phase failures in three-phase three-level inverters. However, because one phase of ESTPIs is directly connected to the neutral point, effectively balancing the neutral point (NP) voltage and reducing the output ripple have been challenging. To address these problems, this article proposes a hybrid model predictive control with vector reconstruction. First, the voltage vectors are reconstructed under unbalanced NP voltage, which eliminates the modeling error term in the cost function, resulting in better steady-state current output and effectively suppressing three-phase unbalance. Subsequently, to eliminate the weighting factors in the cost function, a proportional-differential controller is connected in parallel within the "NP voltage-adjustable sectors" to adjust the vector action time, achieving a hybrid output. Finally, a multistep optimization strategy is proposed, which reduces computation time by approximately 65.8% compared to the preoptimization method. The effectiveness of the proposed method is verified experimentally, demonstrating superior performance over traditional approaches.**

Received 28 June 2025; revised 16 September 2025; accepted 16 October 2025. Date of publication 23 October 2025; date of current version 19 January 2026. This work was supported in part by the National Natural Science Foundation of China under Grant 52377195, in part by the Transformation of Scientific and Technological Achievements in Suzhou (Carbon Peak Carbon Neutral Project) under Grant ST202303, in part by Suzhou Key Laboratory of Smart Energy Technology, in part by Science and Technology Planning Project of Suzhou City under Grant SZS2022015, in part by Natural Science Foundation of the Jiangsu Higher Education Institutions of China under Grant 25KJA470007, in part by "Qing-Lan Project" of Colleges and Universities in Jiangsu Province, and in part by CONICYT Projects under Grant FB0008, Grant ACT192013, and Grant 1170167. Recommended for publication by Associate Editor J. S. Mohamed Ali. *(Corresponding authors: Rong Chen; Yiwang Wang.)*

Yong Yang, Youcheng Wang, and Rong Chen are with the School of Rail Transportation, Soochow University, Suzhou 215131, China (e-mail: yangy1981@suda.edu.cn; suda_wyc@163.com; chrong@suda.edu.cn).

Jiefeng Hu is with the Centre for New Energy Transition Research, Institute of Innovation, Science, and Sustainability, Federation University Australia, Mount Helen, VIC 3353, Australia (e-mail: j.hu@federation.edu.au).

Huiqing Wen is with Xi'an Jiaotong-Liverpool University, Suzhou 215123, China (e-mail: huiqing.wen@xjtlu.edu.cn).

Yiwang Wang is with Suzhou Polytechnic University, Suzhou 211106, China (e-mail: wyw@jssvc.edu.cn).

Hui Yang is with the College of Automation Engineering, Nanjing University of Aeronautics and Astronautics, Nanjing 210096, China (e-mail: yang.hui@nuaa.edu.cn).

Jose Rodriguez is with the Faculty of Engineering, Universidad San Sebastian Santiago, Santiago 8370146, Chile (e-mail: jose.rodriguezp@uss.cl).

Color versions of one or more figures in this article are available at https://doi.org/10.1109/TPEL.2025.3624750.

Digital Object Identifier 10.1109/TPEL.2025.3624750

***Index Terms*—Eight-switch three-phase inverters (ESTPIs), fault-tolerant control, model predictive control, simplified calculation, without weighting factors.**

I. Introduction

COMPARED to traditional two-level inverters, three-phase three-level voltage source inverters (3P-3L VSIs) offer advantages such as lower voltage stress, reduced output current harmonics, and higher efficiency, making them key devices for medium-voltage, high-power applications in industrial applications [1], [2], [3]. However, the inclusion of more power semiconductor devices in 3P-3L VSIs exponentially increases the failure probability [4].

To enhance the stability of 3P-3L VSIs and meet the strict requirements of cost, safety and reliability in modern power electronic systems, fault-tolerant technology has been extensively studied in recent years [5]. Generally, there are many types of faults in power electronic inverters, with semiconductor device faults being among the most common, accounting for approximately 21% of the total [6]. The faults of semiconductor devices can be further divided into short-circuit and open-circuit (OC) faults [7]. Short-circuit faults can cause serious damage to the entire system, necessitating immediate shutdown of the inverters. Conversely, OC faults are primarily caused by thermal cycling, resulting in the lifting and cracking of solder joints within the module. These faults do not typically cause serious safety issues, but result in increased harmonic content in the inverter output current and fluctuations in NP voltage, particularly in three-level inverters with neutral point structure [8], [9].

Several effective strategies have been proposed to address the OC faults in 3P-3L VSIs. For instance, redundant circuits can be added to the inverters to intervene when faults occur [10]. In [11], a normally-closed relay is introduced to improve the voltage gain of the postfault topology. However, the incorporation of additional hardware components increases system cost and complexity. Another approach involves designing the modulation algorithm. However, this method typically requires the design of at least two modulation modes to operate in a hybrid way, which increases the complexity of the algorithm [12]. In [13] active NP voltage imbalance regulation is employed to address external switch faults. However, this method relies on

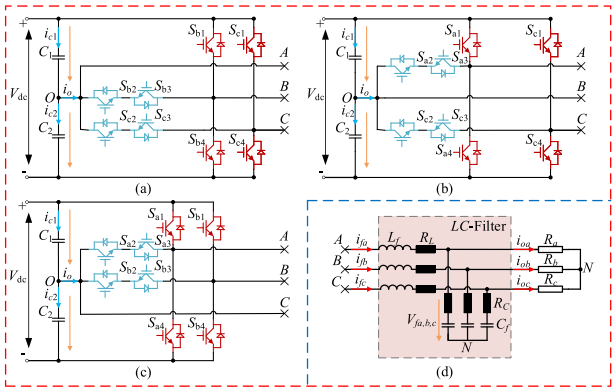

Fig. 1. Circuit structures of ESTPIs. (a) ESTPI-A. (b) ESTPI-B. (c) ESTPI-C. (d) *LC*-filter and loads.

auxiliary front-end rectifiers to introduce new control degrees of freedom. Reconstructing the postfault topology to achieve a new fault-tolerant configuration is relatively economical and easy to implement, which has gained widespread attention among scholars [13], [14], [15].

Eight-switch three-phase inverters (ESTPIs) represent a classic reconstruction topology of 3P-3L VSIs. The reconstruction mode involves directly connecting the faulty phase to the neutral point, thereby forcing the faulty phase into an "O" state. Consequently, there are a total of three possible structures, as depicted in Fig. 1 [16]. However, due to system reconstruction, the maximum modulation ratio and output voltage amplitude will significantly decrease. Therefore, ESTPIs are usually only suitable for low-voltage and low-power applications [17].

For ESTPIs, the direct connection of one phase to the neutral point disturbs the neutral point current, leading to NP voltage unbalance. Unbalanced neutral point (NP) voltage can bring serious problems. For instance, prolonged deviation of NP voltage from the reference value may cause electrolytic capacitor aging or even system breakdown [18]. Furthermore, unbalanced NP voltage also leads to unbalanced three-phase output [19]. Therefore, effectively controlling ESTPIs is a topic worthy of in-depth research. Generally, ESTPIs can be controlled using space-vector pulsewidth modulation (SVPWM) [19], [20], [21], [22]. Liu et al. [20] introduced the carrier-based pulsewidth modulation algorithm and explained its equivalent relationship with SVPWM in [21]. To suppress NP voltage fluctuations, a PI controller is employed for regulating the injection of zero-sequence voltage in [22]. Additionally, in [19], a moving average filter is designed to extract the dc component of the NP voltage to suppress the three-phase unbalance, which serves as compensation for the vector action time. However, these SVPWM-based methods involve complex trigonometric calculations, which are complicated to implement. Moreover, implementing modulation of the unbalanced NP voltage vector action time is complicated.

On the other hand, finite-control-set model predictive control (FCS-MPC) demonstrates significant advantages in addressing such multiobjective optimization problems [23], [24]. First, FCS-MPC establishes the discrete mathematical model of the system, then the prediction equation of the state variables is obtained, and the multiobjective cost function is designed. Finally, the control inputs that minimize the cost function are obtained through rolling optimization. However, conventional FCS-MPC typically applies only one voltage vector per switching cycle, resulting in significant output ripple and variable switching frequency, which complicates filter design [25]. Using multiple voltage vectors offers a viable solution. In [26], three voltage vectors are employed within a single switching cycle, with each vector's duration inversely proportional to its corresponding cost value. Research in [27] has demonstrated that this approach reduces tracking error and maintains a constant switching frequency.

Furthermore, designing an appropriate weighting factor for the cost function is time-consuming. To eliminate the weighting factor for NP voltage balancing, Yang et al. [28] achieved NP voltage balance by adjusting the action time of redundant small voltage vectors. In [29], the weighting factor is eliminated by hierarchical optimization through sequential MPC. Nonetheless, these methods are not applicable for ESTPIs because the reconstructed topology lacks redundant small voltage vectors, and hierarchical optimization results in excessive tracking error. Therefore, to achieve NP voltage balance in ESTPIs, a weighting factor is still used in the cost function in [30]. In [31], virtual zero-vectors are designed to regulate the neutral point current, but their introduction increases the switching loss. In summary, no MPC method for ESTPIs in the existing literature effectively eliminates the weighting factor.

To fill this research gap, this article proposes a hybrid model predictive control (H-MPC) using reconstructed voltage vectors for ESTPIs. The proposed H-MPC eliminates the weighting factor and effectively suppresses the three-phase unbalance. The primary contributions of this research are outlined as follows.

1) *Weighting-Free NP Voltage Control:* This work introduces a novel parallel control architecture that integrates a proportional-differential (PD) controller with MPC, effectively eliminating the need for weighting factor tuning in the cost function. By dynamically adjusting vector dwell times exclusively in NP voltage adjustable sectors through real-time analysis of small voltage vectors' impact on NP current, the method achieves robust voltage balancing without compromising control performance.
2) *NP Voltage-Compensated Vector Reconstruction:* The impact of NP voltage imbalance on modeling errors is rigorously analyzed. A real-time voltage vector reconstruction mechanism is developed to compensate for these errors, significantly improving steady-state performance. This method suppresses three-phase current unbalance and keeps THD below 4.0%, even under significant NP voltage deviations.
3) *Computationally Efficient Multistep Optimization:* A streamlined multistep optimization strategy is proposed. By prescreening and prioritizing voltage vectors based on the sector classification, the computational burden is reduced by approximately 65.8% compared to the exhaustive search method, making the proposed algorithm more practical for real-time implementation.

The rest of this article is organized as follows. Section II provides a comprehensive description of the overall system model and dynamic model. In Section III, the proposed H-MPC is

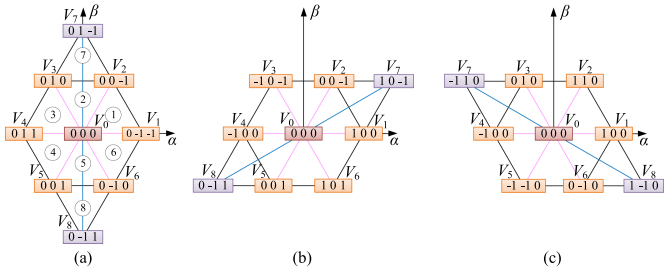

Fig. 2 Space vector diagram for different ESTPIs. (a) ESTPI-A. (b) ESTPI-B. (c) ESTPI-C.

detailed. Section IV presents various comparative experimental results. Finally, Section V concludes this article.

II. System Modeling and Traditional FCS-MPC

The circuit structures of the three ESTPIs with an *LC*-filter are shown in Fig. 1 [19].

As depicted, $V_{\rm dc}$ is the dc voltage, and V_p and V_n represent the voltages of the upper and lower capacitors, respectively. In the equilibrium state, $V_p = V_n = V_{\rm dc}/2$. $ic1$, $ic2$, and i_o represent the currents flowing through the upper and lower capacitors and the neutral point current, respectively. L_f, R_L, C_f, and R_C constitute the output *LC*-filter. $i_{fx}(x = a, b, c)$ is the current of the filter inductor, while $V_{fx}(x = a, b, c)$ and $i_{ox}(x = a, b, c)$ represent the voltage of the filter capacitor and output current, respectively. R_a, R_b, and R_c represent phase-A, phase-B, and phase-C linear resistive loads, respectively.

The three structures are essentially equivalent, so ESTPI-A is used as an example for modeling and analyzing without loss of generality.

A. General ESTPI-A Model

For a nonfaulty T-type 3P-3L VSI, each leg can output three possible output states, which are denoted as "P," "O," and "N", where "P" signifies that the power switches $S_{x1}(x = a, b, c)$ and $S_{x2}(x = a, b, c)$ are turned ON, "O" means that the power switches $S_{x2}(x = a, b, c)$ and $S_{x3}(x = a, b, c)$ are turned ON, and "N" indicates that the power switches $S_{x3}(x = a, b, c)$ and $S_{x4}(x = a, b, c)$ are turned on. Since ESTPIs connect the faulted phase directly to the neutral point, only 9 possible voltage vectors exist for each ESTPI, as shown in Fig. 2 [30].

For ESTPI-A, the switching function S_x for phase-B and phase-C can be defined as

$$S_x = \begin{cases} 1 & S_{x1} \text{ and } S_{x2} \text{ on, } S_{x3} \text{ and } S_{x4} \text{ off} \\ 0 & S_{x2} \text{ and } S_{x3} \text{ on, } S_{x1} \text{ and } S_{x4} \text{ off} \\ -1 & S_{x3} \text{ and } S_{x4} \text{ on, } S_{x1} \text{ and } S_{x2} \text{ off} \end{cases} \quad x = b, c. \tag{1}$$

Assuming the NP voltage is already effectively balanced, the output voltage of each phase with respect to the neutral point "*O*" can be expressed as follows:

$$\begin{bmatrix} V_{aO} \\ V_{bO} \\ V_{cO} \end{bmatrix} = \begin{bmatrix} 0 & 0 & 0 \\ 0 & V_{\rm dc}/2 & 0 \\ 0 & 0 & V_{\rm dc}/2 \end{bmatrix} \begin{bmatrix} 0 \\ S_b \\ S_c \end{bmatrix}. \tag{2}$$

Furthermore, the output voltage of each phase with respect to the load neutral point "*N*" can be expressed as follows:

$$\begin{bmatrix} V_{aN} \\ V_{bN} \\ V_{cN} \end{bmatrix} = \frac{1}{3} \begin{bmatrix} 2 & -1 & -1 \\ -1 & 2 & -1 \\ -1 & -1 & 2 \end{bmatrix} \begin{bmatrix} V_{aO} \\ V_{bO} \\ V_{cO} \end{bmatrix} \tag{3}$$

and the synthesized voltage vector $V_o$can be expressed as [28]

$$V_o = \frac{2}{3}(V_{aN} + \gamma V_{bN} + \gamma^2 V_{cN}) \tag{4}$$

where $\gamma = e^{j2\pi/3}$.

According to Kirchhoff's law, assuming three phases are symmetrical, the circuit equation in Fig. 1(a) can be derived as follows:

$$\begin{bmatrix} V_{aN} \\ V_{bN} \\ V_{cN} \end{bmatrix} = L_f \frac{d}{dt} \begin{bmatrix} i_{fa} \\ i_{fb} \\ i_{fc} \end{bmatrix} + R_L \begin{bmatrix} i_{fa} \\ i_{fb} \\ i_{fc} \end{bmatrix} + \begin{bmatrix} V_{fa} \\ V_{fb} \\ V_{fc} \end{bmatrix}. \tag{5}$$

Setting the inductor current $i_{fx}(x = a, b, c)$ as a state variable, the model in (5) can be transformed into a two-phase stationary coordinate system through Clarke transformation, expressed as follows:

$$L_f \frac{d}{dt} \begin{bmatrix} i_{f\alpha} \\ i_{f\beta} \end{bmatrix} = \begin{bmatrix} V_\alpha \\ V_\beta \end{bmatrix} - R_L \begin{bmatrix} i_{f\alpha} \\ i_{f\beta} \end{bmatrix} - \begin{bmatrix} V_{f\alpha} \\ V_{f\beta} \end{bmatrix}. \tag{6}$$

If the operation time is significantly shorter than the period of the output current, the forward Euler approximation is used to discretize the continuous model. Consequently, the recursive expression of the state variable at the $(k+1)$th and (k)th instants can be obtained, and the discrete state-space model of (6) is as follows:

$$\begin{cases} i_{f\alpha}(k+1|k) = i_{f\alpha}(k) + \frac{T_s}{L_f}\left(V_\alpha(k) - R_L i_{f\alpha}(k) - V_{f\alpha}(k)\right) \\ i_{f\beta}(k+1|k) = i_{f\beta}(k) + \frac{T_s}{L_f}\left(V_\beta(k) - R_L i_{f\beta}(k) - V_{f\beta}(k)\right) \end{cases}. \tag{7}$$

It is worth noting that all the aforementioned models are based on the balanced NP voltage. In practice, the NP voltage needs to be analyzed. As shown in Fig. 1, the relationship between the current and voltage of the upper and lower capacitors on the dc side can be expressed as follows:

$$\begin{cases} i_{c1} = C_1 \frac{dV_p}{dt} \\ i_{c2} = C_2 \frac{dV_n}{dt} \end{cases}. \tag{8}$$

The balance of NP voltage is related to the neutral point current i_o, which can be expressed as follows:

$$i_o = i_{fa}(1 - |S_a|) + i_{fb}(1 - |S_b|) + i_{fc}(1 - |S_c|). \tag{9}$$

Similarly, (8) can be discretized using the forward Euler method. Thus, the difference between the voltage of the upper and lower capacitors at the $(k+1)$th instant can be obtained

$$\begin{aligned} \Delta V_{NP}(k+1|k) &= V_p(k+1|k) - V_n(k+1|k) \\ &= (V_p(k) - V_n(k)) + \frac{T_s}{C} i_o(k) \\ &= \Delta V_{NP}(k) + \frac{T_s}{C} \sum_{x \in \{a,b,c\}} (1 - |S_x|) i_{fx}(k) \end{aligned} \tag{10}$$

where $C_1 = C_2 = C$.

B. Traditional FCS-MPC

To achieve accurate reference current tracking and NP voltage balancing, the cost function of FCS-MPC is expressed as follows:

$$J_0\left(V_c\right)=\sum_{i=2}^{p}\left\|\boldsymbol{\Gamma}_y\left(\boldsymbol{Y}_c\left(k+i|k\right)-\boldsymbol{R}\left(k+i\right)\right)\right\|^2 \tag{11}$$

considering the one-step delay compensation inherent in FCS-MPC and the reduced prediction accuracy due to multistep prediction ($p=2$), and the weighting factor matrix, the prediction matrix and the reference matrix are denoted as

$$\boldsymbol{\Gamma}_y=diag\left(1,1,\lambda\right) \tag{12}$$

$$\boldsymbol{Y}_c\left(k+i|k\right)=\left[i_{f\alpha}(k+i|k)\quad i_{f\beta}\left(k+i|k\right)\quad \Delta V_{NP}\left(k+i|k\right)\right]^T \tag{13}$$

$$\boldsymbol{R}\left(k+i\right)=\left[i^*_{f\alpha}\left(k+i\right)\quad i^*_{f\beta}\left(k+i\right)\quad 0\right]^T \tag{14}$$

where λ is the weighting factor for NP voltage balancing, the prediction matrix is obtained from (7) and (10). $i^*_{f\alpha}(k+i)$ and $i^*_{f\beta}(k+i)$ represent the reference values for inductive current, which can be calculated using Lagrange interpolation. For sinusoidal reference, the order "n" should not be less than 2 [26]. Consequently, the reference values for inductive current in the $\alpha\beta$ system can be expressed as follows:

$$\begin{cases} i^*_{f\alpha}\left(k+i\right)=3i^*_{f\alpha}\left(k+i-1\right)-3i^*_{f\alpha}\left(k+i-2\right) \\ \qquad\qquad +i^*_{f\alpha}\left(k+i-3\right) \\ i^*_{f\beta}\left(k+i\right)=3i^*_{f\beta}\left(k+i-1\right)-3i^*_{f\beta}\left(k+i-2\right) \\ \qquad\qquad +i^*_{f\beta}\left(k+i-3\right) \end{cases}. \tag{15}$$

Each voltage vector corresponds to a specific cost value. Therefore, through rolling optimization, the voltage vector minimizing the cost function is determined and employed for the next switching cycle, which can be expressed as

$$V_{opt}=\arg\min_{i\in\{0,1,2,3,4,5,6,7,8\}}J_0(V_i). \tag{16}$$

III. Proposed H-MPC Algorithm

In this section, a H-MPC is proposed. First, to reduce output ripple and achieve a fixed switching frequency, the H-MPC applies three voltage vectors within one switching cycle, with their respective action times inversely proportional to the corresponding cost values. Subsequently, the prediction error and three-phase unbalance due to unbalanced NP voltage are analyzed, and the voltage vectors are reconstructed based on the actual NP voltage. Finally, hybrid modulation is realized by a PD regulator that adjusts the vector action time within the "NP voltage adjustable sectors". The specific technical details are elucidated as follows.

A. Reduced Current Ripple

Conventional FCS-MPC usually operates only one voltage vector during one switching cycle, which can introduce large output ripples that are undesirable in modern power systems. To address this problem, most existing articles suggest the use of modulation, which effectively reduces the output ripple.

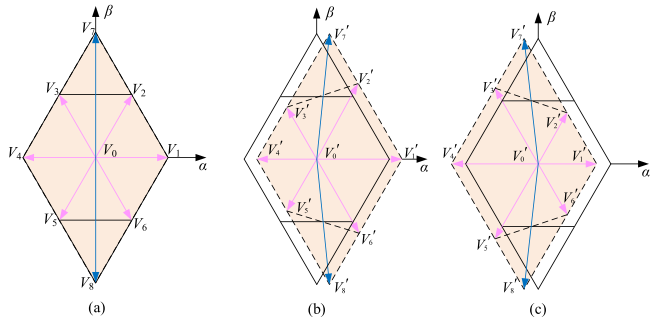

Fig. 3. Voltage vectors under different NP voltage conditions for ESTPI-A. (a) $\zeta=0$. (b) $\zeta<0$. (c) $\zeta>0$.

Therefore, in this article, referring to [28], the space vector is divided into 8 triangular feasible sectors, and 3 voltage vectors are applied in one switching cycle. The final synthesized voltage vector can be expressed as follows:

$$V_{sv}=\frac{t_m}{T_s}V_m+\frac{t_n}{T_s}V_n+\frac{t_z}{T_s}V_z \tag{17}$$

where the action times of the three voltage vectors are inversely proportional to the corresponding tracking costs, which can be defined as follows:

$$J_t\left(V_i\right)=\left(i^*_{f\alpha}\left(k+2\right)-i_{f\alpha}\left(k+2|k\right)\right)^2 + \left(i^*_{f\beta}\left(k+2\right)-i_{f\beta}\left(k+2|k\right)\right)^2 i=0,1\cdots 8. \tag{18}$$

Then, t_m, t_n, and t_z can be expressed as

$$\begin{cases} t_m=\frac{J_t(V_n)J_t(V_z)}{J_t(V_m)J_t(V_n)+J_t(V_m)J_t(V_z)+J_t(V_n)J_t(V_z)}T_s \\ t_n=\frac{J_t(V_m)J_t(V_z)}{J_t(V_m)J_t(V_n)+J_t(V_m)J_t(V_z)+J_t(V_n)J_t(V_z)}T_s \\ t_z=T_s-t_m-t_n. \end{cases} \tag{19}$$

The above modulation method can effectively reduce current ripple, but it can also introduce a high computational burden. Therefore, further optimization of the method will be analyzed.

B. Reconstruction of Voltage Vectors Under Unbalanced NP Voltage

For ESTPIs, since one phase is directly connected to the neutral point, NP voltage fluctuation is unavoidable and always fluctuates around the equilibrium point, resulting in a dynamic balance. However, when the NP voltage fluctuation is large, it causes significant output ripple and even three-phase unbalance.

To analyze this problem, the degree of unbalance is defined as follows [22]:

$$\xi=\frac{V_p-V_n}{V_{\rm dc}}. \tag{20}$$

When $V_p\neq V_n\neq V_{\rm dc}/2$, (2) needs to be rewritten according to the actual NP voltage to obtain the exact voltage vectors, as summarized in Table I. Furthermore, voltage vectors under different NP voltage conditions for ESTPI-A are shown in Fig. 3.

TABLE I
ACCURATE VOLTAGE VECTORS BASED ON NP VOLTAGE

Voltage Vectors	ESTPI-A	ESTPI-B	ESTPI-C
(0 0)	0	0	0
(-1 -1)	$2V_n/3$	$V_n(-1/3+j\sqrt{3}/3)$	$V_p(-1/3-j\sqrt{3}/3)$
(0 -1)	$V_n(1/3+j\sqrt{3}/3)$	$V_n(1/3+j\sqrt{3}/3)$	$V_p(1/3-j\sqrt{3}/3)$
(1 0)	$V_n(-1/3+j\sqrt{3}/3)$	$2V_n/3$	$2V_n/3$
(1 1)	$-2V_p/3$	$V_p(1/3-j\sqrt{3}/3)$	$V_n(1/3+j\sqrt{3}/3)$
(0 1)	$V_p(-1/3-j\sqrt{3}/3)$	$V_p(-1/3-j\sqrt{3}/3)$	$V_n(-1/3+j\sqrt{3}/3)$
(-1 0)	$V_p(1/3-j\sqrt{3}/3)$	$-2V_p/3$	$-2V_p/3$
(1 -1)	$(V_n-V_p)/3+j\sqrt{3}(V_p+V_n)/3$	$2V_p/3+V_n/3+j\sqrt{3}V_n/3$	$2V_p/3-V_n/3+j\sqrt{3}V_n/3$
(-1 1)	$(V_n-V_p)/3-j\sqrt{3}(V_p+V_n)/3$	$-V_p/3-2V_n/3-j\sqrt{3}V_n/3$	$-2V_n/3+V_p/3-j\sqrt{3}V_p/3$

It can be observed that when $\zeta \neq 0$, the voltage vectors deviate from their original positions, generating modeling errors.

Therefore, the relationship between the voltage vectors $\boldsymbol{V}_{\alpha\beta}(k+1)$ substituted into (11) and the actual voltage vectors $\boldsymbol{V'}_{\alpha\beta}(k+1)$ can be expressed as follows:

$$\begin{bmatrix} V_\alpha(k+1) \\ V_\beta(k+1) \end{bmatrix} = \begin{bmatrix} V'_\alpha(k+1) \\ V'_\beta(k+1) \end{bmatrix} + \boldsymbol{E}_u(k+1) \tag{21}$$

where $\boldsymbol{E}_u$ represent the modeling error due to unbalanced NP voltage, and $|\boldsymbol{E}_u| \propto |\xi|$.

Substituting (21) into (7), the current prediction error can be obtained

$$\begin{aligned} \boldsymbol{E}_i(k+2) &= \boldsymbol{i}_{\alpha\beta}(k+2) - \boldsymbol{i'}_{\alpha\beta}(k+2) \\ &= \frac{T_s}{L_f}\left(\boldsymbol{V}_{\alpha\beta}(k+1) - \boldsymbol{V'}_{\alpha\beta}(k+1)\right) = \frac{T_s}{L_f}\boldsymbol{E}_u(k+1). \end{aligned} \tag{22}$$

Substituting (22) into (11), the imprecise cost value due to the imprecise voltage vectors can be expressed as

$$\begin{aligned} J_0^{Err} &= \left(i^*_{f\alpha}(k+2) - i'_\alpha(k+2\,|\,k)\right)^2 \\ &+ \left(i^*_{f\beta}(k+2) - i'_\beta(k+2\,|\,k)\right)^2 \\ &+ \lambda\Delta V_{NP}^2(k+2\,|\,k) + \frac{T_s^2\left(E_{u\alpha}^2(k+1) + E_{u\beta}^2(k+1)\right)}{L_f^2} \\ &- \frac{2T_sE_{u\alpha}(k+1)}{L_f}\left(i^*_{f\alpha}(k+2) - i'_\alpha(k+2\,|\,k)\right) \\ &- \frac{2T_sE_{u\beta}(k+1)}{L_f}\left(i^*_{f\beta}(k+2) - i'_\beta(k+2\,|\,k)\right). \end{aligned} \tag{23}$$

From (21), (22), and (23), it can be seen that the unbalanced NP voltage superimposes a perturbation term on the correct cost function. This perturbation affects the optimization process, causing the controller to output an erroneous control quantity, which is the root cause of output current distortion and three-phase unbalance.

To eliminate this effect, one approach is to adjust the voltage vector action time to correct the voltage vector offset caused by the NP voltage. However, this approach is complex and not well-suited for MPC. Therefore, this article proposes a more intuitive method that directly calculates the exact values of all voltage vectors according to Table I, and uses them as inputs to MPC. This method eliminates the perturbation term in (23), ensuring the correct control quantities are obtained.

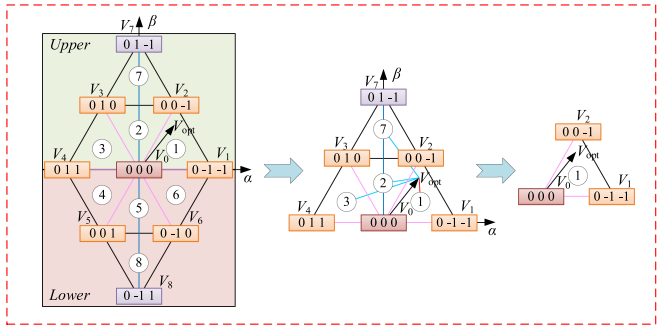

Fig. 4. Proposed multistep optimization method.

The voltage vectors reconstruction of ESTPI-A can be expressed as follows:

$$\begin{bmatrix} V'_0 \\ V'_1 \\ V'_2 \\ V'_3 \\ V'_4 \\ V'_5 \\ V'_6 \\ V'_7 \\ V'_8 \end{bmatrix} = \begin{bmatrix} 0 & 0 \\ 0 & 2/3 \\ 0 & 1/3+j\sqrt{3}/3 \\ 0 & -1/3+j\sqrt{3}/3 \\ -2/3 & 0 \\ -1/3-j\sqrt{3}/3 & 0 \\ 1/3-j\sqrt{3}/3 & 0 \\ -1/3+j\sqrt{3}/3 & 1/3+j\sqrt{3}/3 \\ -1/3-j\sqrt{3}/3 & 1/3-j\sqrt{3}/3 \end{bmatrix} \begin{bmatrix} V_p \\ V_n \end{bmatrix}. \tag{24}$$

Equation (24) can also be extended to ESTPI-B and ESTPI-C as required.

C. Proposed Multistep Optimization Method

To achieve fast optimization, a multistep optimization method is proposed in this section.

As shown in Fig. 2(a), the whole space sector can be regarded as a symmetric rhombus. First, the large triangle subsector is determined based on the 2 large voltage vectors ((01, −1) and (0, −11)), as illustrated in Fig. 4. Subsequently, to further

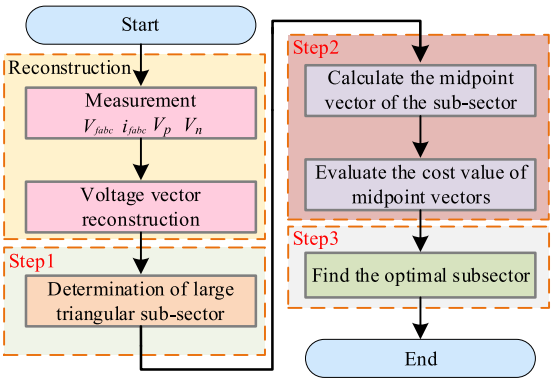

Fig. 5. Flowchart of the vector reconstruction and multistep optimization method.

determine the small triangle sector, the cost value of each voltage vector located at the midpoint of the small triangle sector is evaluated. This evaluation identifies the sector where the voltage vector that minimizes the cost function is located, which becomes the final output of the small triangle sector.

The above optimization method is equally applicable to ESTPI-B and ESTPI-C. It is worth noting that the weighting term of the NP voltage is not considered in the optimization process, as it will be eliminated in subsequent analysis.

In summary, Fig. 5 illustrates the implementation process of the proposed voltage vector reconstruction and multistep optimization method.

In microprocessor based digital MPC algorithms, the computational time complexity of the algorithm can be effectively evaluated by quantifying the number of multiplication and division operations required. Compared to the traditional eight-sector optimization method, the proposed method uses a multistep computation strategy and requires only 72 multiplication operations and two division operations, whereas the traditional method requires 198 multiplication operations and 16 division operations. These results demonstrate that the proposed approach significantly improves computational efficiency and reduces the overall computation time.

D. NP Voltage Balance

For ESTPIs, due to the absence of redundant small voltage vectors, NP voltage balance cannot be achieved by adjusting the action time of redundant small voltage vectors, as is possible with 3P-3L VSIs [30]. To address this issue, a feasible alternative is to control the charging and discharging of the upper and lower capacitors by adjusting the neutral point current.

Table II summarizes the neutral point current corresponding to the nine voltage vectors of ESTPI-A. Since each small triangle sector designed in this article contains two small voltage vectors, these small triangular sectors can be classified into "NP voltage adjustable sectors" and "NP voltage nonadjustable sectors" by analyzing the neutral point current corresponding to the two small voltage vectors. Specifically, when the neutral point currents corresponding to the two small voltage vectors in a small triangular sector are in opposite directions, it is considered an

TABLE II
NEUTRAL POINT CURRENT OF DIFFERENT VOLTAGE VECTORS FOR ESTPI-A

Voltage Vectors	NP current	Voltage Vectors	NP current
$V_0(0, 0, 0)$	0	$V_5(0, 0, 1)$	$-i_{fc}$
$V_1(0, -1, -1)$	i_{fa}	$V_6(0, -1, 0)$	$-i_{fb}$
$V_2(0, 0, -1)$	$-i_{fc}$	$V_7(0, 1, -1)$	i_{fa}
$V_3(0, 1, 0)$	$-i_{fb}$	$V_8(0, -1, 1)$	i_{fa}
$V_4(0, 1, 1)$	i_{fa}	——	——

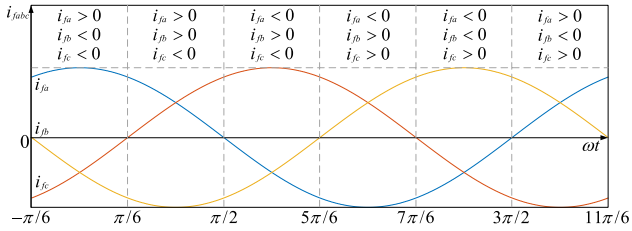

Fig. 6. Relationship between three-phase current direction and sectors.

"NP voltage adjustable sector"; otherwise, it is an "NP voltage nonadjustable sector".

During steady-state, it is assumed that the inductor current accurately tracks the reference current. Fig. 6 illustrates the three-phase current directions versus the space vectors. Combined with Table II, it can be seen that only the small triangle sectors 2, 5, 7, and 8 are "NP voltage adjustable sectors", while the small triangle sectors 1, 3, 4, and 6 are "NP voltage nonadjustable sectors".

Therefore, time compensation is only required in the "NP voltage adjustable sectors". For example, when $V_p > V_n$, the operation time of the two small voltage vectors are t_m and t_n with $i_m > 0$ and $i_n < 0$. The compensation time is t, and the post-compensation time can be expressed as follows:

$$\begin{cases} t'_m = t_m + t & i_m > 0 \\ t'_n = t_n - t & i_n < 0 \\ \text{s.t. } 0 \le t \le \text{Min}\,(t_m, t_n)\,. \end{cases} \tag{25}$$

Then, the equivalent i_0 can be expressed as

$$i_0 = \frac{t'_m}{T_s} i_m + \frac{t'_n}{T_s} i_n = C \frac{d(\xi V_{\text{dc}})}{dt}. \tag{26}$$

Assuming that dc-link voltage V_{dc} is constant, (26) can be further transformed into the s domain as follows [24]:

$$\frac{\xi(s)}{i_0(s)} = \frac{1}{C V_{\text{dc}} s}. \tag{27}$$

It can be seen from (27), the unbalance degree ζ can be regulated by controlling the neutral point current i_0. Furthermore, from (25) and (26), i_0 can be adjusted by the compensation time t. To simplify the control algorithm, the regulation process of ζ can be considered as a positional PID control. To eliminate the over-regulation caused by the integral component, a PD controller can be used instead. The closed-loop control block diagram is shown in Fig. 7.

In addition, to avoid excessive NP voltage fluctuation, the reference value of ζ for sector 2 can be slightly larger than 0, as

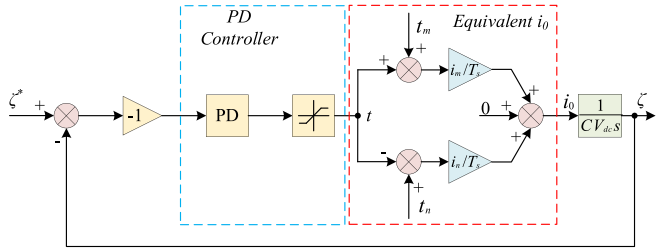

Fig. 7. Closed-loop control block diagram of ζ.

sectors 3 and 4 always decrease ζ. Similarly, the reference value of ζ for sector 5 can be slightly smaller than 0.

E. Comparison With Weighting Factors

Although the PD controller-based NP voltage balancing method proposed in this work eliminates weighting factors in the cost function, it still requires parameter tuning for the controller gains. However, this approach offers distinct advantages compared to weighting factor-based methods.

As the analysis demonstrates, not all subsectors possess bidirectional NP voltage regulation capability. Consequently, weighting factor-based methods must evaluate all subsectors to balance control objectives, resulting in excessive computational burden and potential performance compromises when NP voltage deviations force selection of voltage-regulating subsectors over those with minimal tracking error, ultimately increasing output ripple.

The proposed solution employs PD controllers to decouple reference tracking from NP voltage control, limiting vector action time compensation exclusively to "NP voltage adjustable sectors". This targeted approach minimizes steady-state impacts on output current while maintaining voltage balance, thereby achieving superior steady-state performance compared to conventional weighting factor-based control.

F. System Overall Control

Based on the preceding analysis, the overall control block diagram of the proposed H-MPC is illustrated in Fig. 8.

IV. Experimental Results

Experiments were conducted to validate the superiority and adaptability of the proposed H-MPC in this article. As shown in Fig. 9, an ESTPI experiment platform was built based on a Texas Instruments DSP chip (TMS320F28374S), where inductor current ($i_{fa,b,c}$) and output current ($i_{oa,b,c}$) are sampled by current sensors, and output voltage ($V_{oa,b,c}$) and NP voltage ($V_{p,n}$) are sampled by LEM voltage sensors. For dc side, two dc power sources (MAISHENG-MP3003D) were used in series for power supply. The experimental waveforms were captured using an oscilloscope (TEK-MDO3054). Additionally, voltage probes (PINTECH-N1015B) and current probes (TEK-TCPA3000, TEK-TCP300) were used to measure the voltage and current signals. The DSP executed control algorithms. Essential parameters are detailed in Table III.

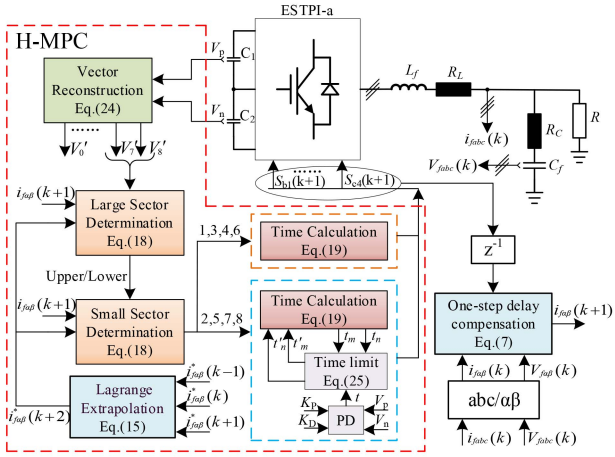

Fig. 8. Overall system control block diagram.

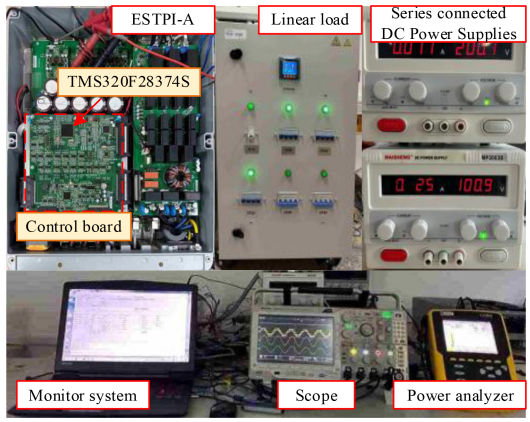

Fig. 9. System experiment platform.

TABLE III
Parameters of the System

Variable	Description	Numeric Value
V_{dc}	Dc voltage	300[V]
T_s	Sampling and control period	62.5[us]
C_1, C_2	Dc-link Capacitors	500[uF]
$R_{a,b,c}$	Linear loads	12[Ω]
L_f	Filter inductor	5[mH]
R_L	Inductive parasitic resistance	0.05[Ω]
C_f	Filter capacitor	20[uF]
f	Rated output frequency	50[Hz]

The experimental setup assumes an open-circuit fault condition in the A-phase bridge arm, leading to hardware reconfiguration as an ESTPI-A. It should be noted that all subsequent experimental results and performance evaluations are based on this ESTPI-A configuration.

What is more, three algorithms are implemented and compared on the experimental platform, each defined as follows.

Traditional MPC (T-MPC): For traditional MPC, the cost function is designed as (11). For fair experimentation, the THD of the output current and NP voltage fluctuations were compared under different weighting factors, and the weighting factor λ

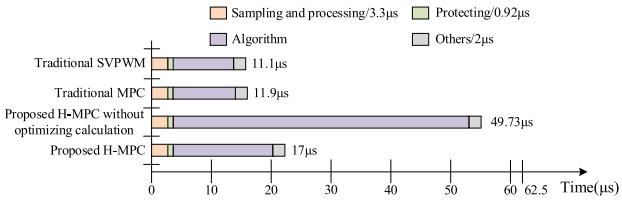

Fig. 10. Comparison of time complexity of different algorithms.

was finally set to 0.15. The optimal voltage vector is obtained by evaluating nine voltage vectors.

Traditional SVPWM (T-SVPWM): Traditional SVPWM uses a closed-loop control strategy with *d-q* current decoupling, where $k_p = 0.8$ and $k_i = 0.02$. Meanwhile, NP voltage balance is achieved by zero-sequence voltage injection.

H-MPC: The proposed MPC algorithm with $k_p = 0.6$ (tunable range: 0.48-0.84) and $k_d = 0.3$ (tunable range: 0.18-0.78).

The test conditions are listed as follows.

Condition 1: The amplitude and frequency of the reference current are set to 3 A and 50 Hz with $R_{abc} = 12\,\Omega$, respectively.

Condition 2: The amplitude and frequency of the reference current are set to 5 A and 50 Hz with $R_{abc} = 12\,\Omega$, respectively.

Condition 3: The frequency of the reference current is set to 50 Hz and the amplitude jumps from 3 A to 5 A with $R_{abc} = 12\,\Omega$.

Condition 4: The frequency of the reference current is set to 50 Hz and the amplitude jumps from 5 A to 3 A with $R_{abc} = 12\,\Omega$.

Condition 5: The amplitude and frequency of the reference current are set to 3 A and 50 Hz with $R_{abc} = 12\,\Omega$, respectively. A 40 V dc offset is injected into the NP voltage.

Condition 6: The amplitude and frequency of the reference current are set to 3 A and 50 Hz with $R_{abc} = 12\,\Omega$, respectively. Filter inductor L_f and parasitic resistance R_L change $\pm 50\%$, respectively.

A. Execution Time

First of all, the time complexity of the three methods is compared using a DSP-TMS320F28374S with a crystal frequency of 200 MHz and a sampling period of 62.5 μs.

Specifically, the execution time of A/D conversion, system protection and other tasks is about 6.22 μs, and the rest is the execution time of the three methods. In addition, to highlight the superiority of the proposed multistep optimization method, experiments were also conducted with an unoptimized method that calculates the cost value for each small sector.

The experimental results are depicted in Fig. 10. The computation time for T-SVPWM is 11.1 μs, for T-MPC is 11.9 μs, and for the proposed H-MPC is 17 μs. Due to the introduction of modulation and cost function calculation, the computation time of MPC-based methods is greater than that of T-SVPWM. Notably, the multistep optimization method proposed in this article reduces the computation time by approximately 65.8% compared to the unoptimized method.

The experimental results demonstrate that the proposed multistep optimization method significantly reduces the computational burden.

B. Steady-State Performance Evaluation

Fig. 11 illustrates the steady-state experimental waveforms for the three methods under Condition 1 and Condition 2. The experimental results demonstrate that all three methods effectively track the reference current. In terms of NP voltage fluctuation, T-MPC and H-MPC exhibit slightly smaller fluctuations compared to T-SVPWM.

Furthermore, Fig. 12 presents the harmonic spectra of the output current, generated using MATLAB/Simulink with experimental data acquired from the oscilloscope. The total harmonic distortion (THD) corresponding to T-MPC, T-SVPWM and H-MPC are 11.2%, 4.3%, and 3.52% under Condition 1, respectively. Under Condition 2, the THD of the three methods are 6.9%, 2.98% and 2.71%, respectively. The experimental results indicate that H-MPC has the lowest THD across different reference current amplitudes, demonstrating that the vector reconstruction strategy proposed in this article effectively reduces the impact of NP voltage fluctuation.

In addition, both T-SVPWM and H-MPC maintain a constant switching frequency. The high harmonics of the output current are primarily concentrated at the sampling frequency and its multiples, such as 16 kHz and 32 kHz. However, the high harmonics of T-MPC are dispersed across a range of frequencies, complicating filter design.

C. Dynamic Performance Evaluation

In this section, the dynamic performance of the three methods is evaluated under Condition 3 and Condition 4, respectively. The experimental results are shown in Fig. 13, and the following conclusions can be drawn.

1) When the reference current amplitude changes, all three methods can quickly track the given reference. However, under Condition 3, T-SVPWM exhibits overshoot due to the PI controller, indicating that the dynamic performance of T-MPC and H-MPC is slightly better than that of T-SVPWM.
2) In terms of NP voltage fluctuation, under Condition 3 and Condition 4, the voltage fluctuations for T-MPC and H-MPC are approximately 8 V. In contrast, the NP voltage fluctuation for T-SVPWM is about 12 V under Condition 3. This indicates that T-MPC and H-MPC perform better in suppressing NP voltage fluctuation.

D. Three-Phase Unbalance Suppression Experiments

To further evaluate the suppression ability of the three methods against output current unbalance when NP voltage is unbalanced, the experimental condition is set to Condition 5. The experimental results are shown in Fig. 14. From these results, it can be seen that when the NP voltage is unbalanced, both T-MPC and T-SVPWM exhibit three-phase unbalance and output current distortion. In contrast, the H-MPC proposed in this article maintains better three-phase balance and sinusoidal current output.

In addition, to verify the effectiveness of the proposed vector reconfiguration method, experiments were conducted on

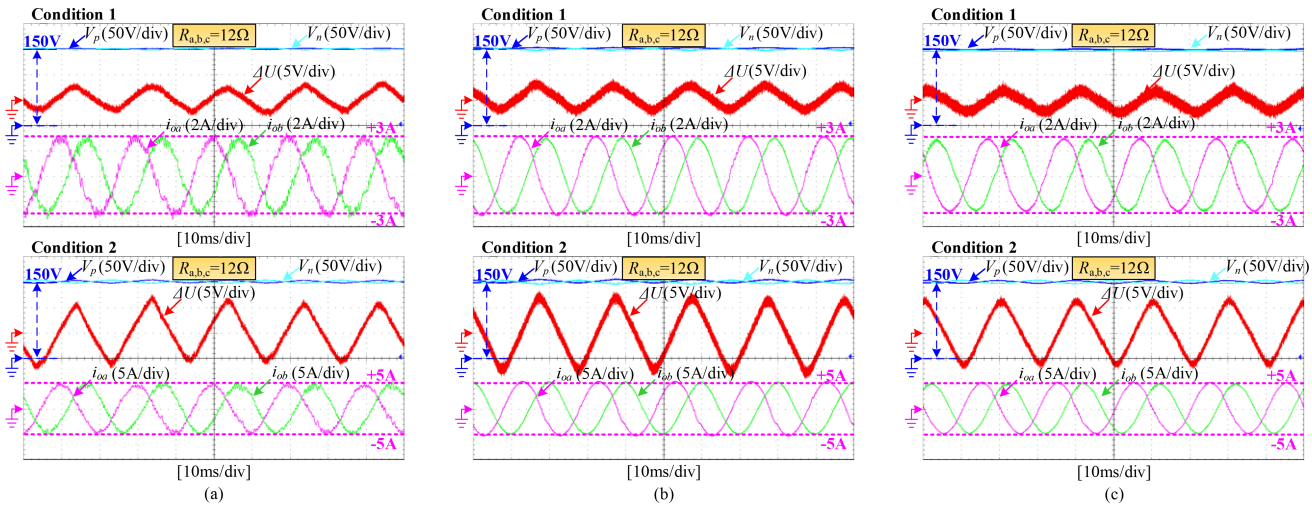

Fig. 11. Steady-state experimental waveforms under Condition 1 and Condition 2. (a) T-MPC. (b) T-SVPWM. (c) Proposed H-MPC.

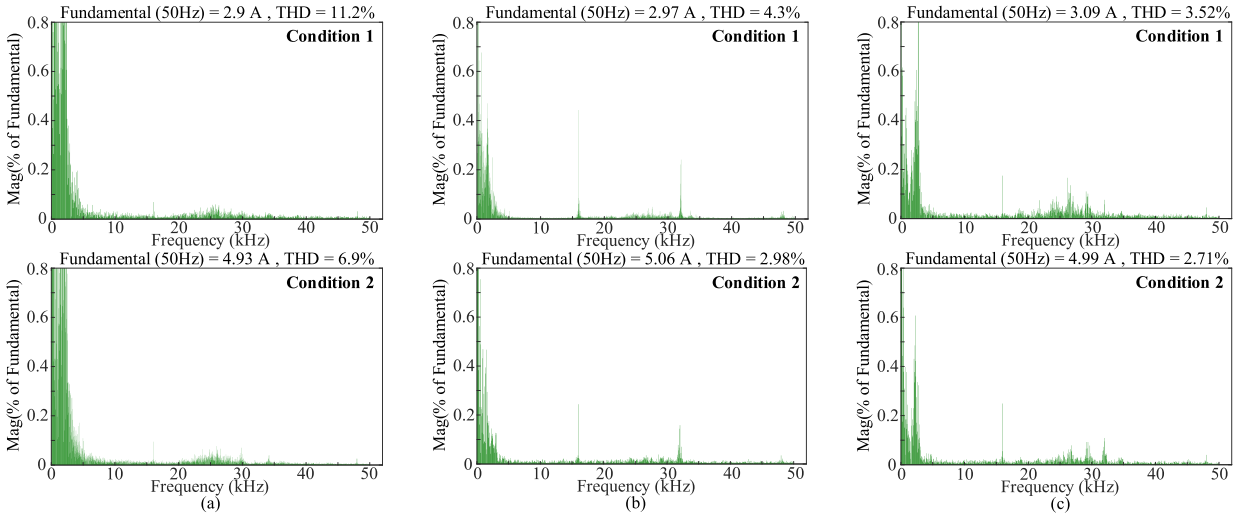

Fig. 12. FFT analysis of steady-state experiments under Condition 1 and Condition 2. (a) T-MPC. (b) T-SVPWM. (c) Proposed H-MPC.

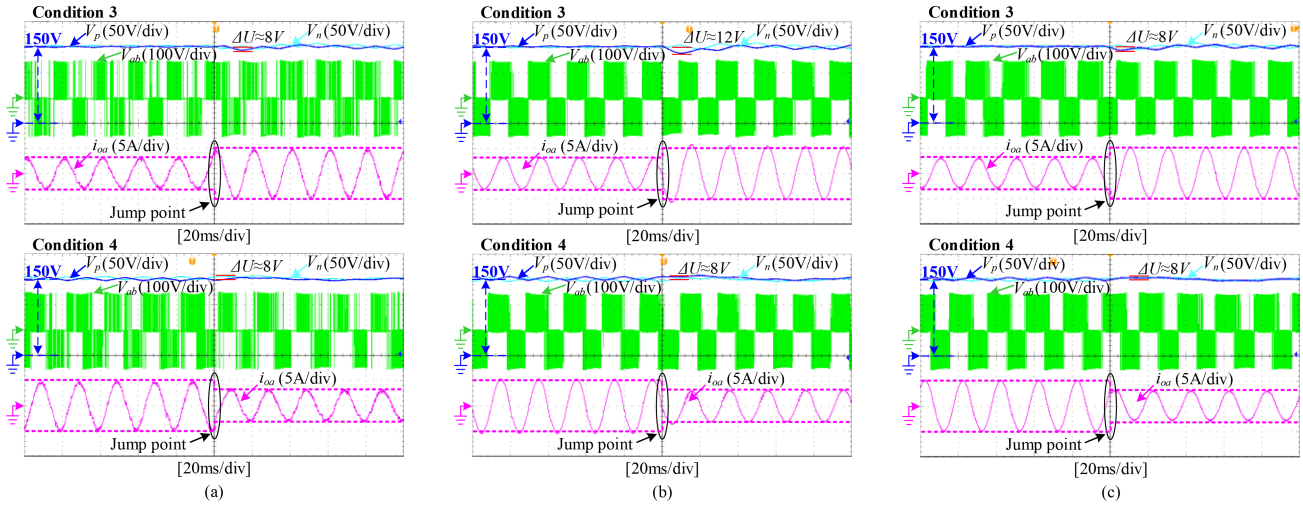

Fig. 13. Dynamic experimental waveforms under Condition 3 and Condition 4. (a) T-MPC. (b) T-SVPWM. (c) Proposed H-MPC.

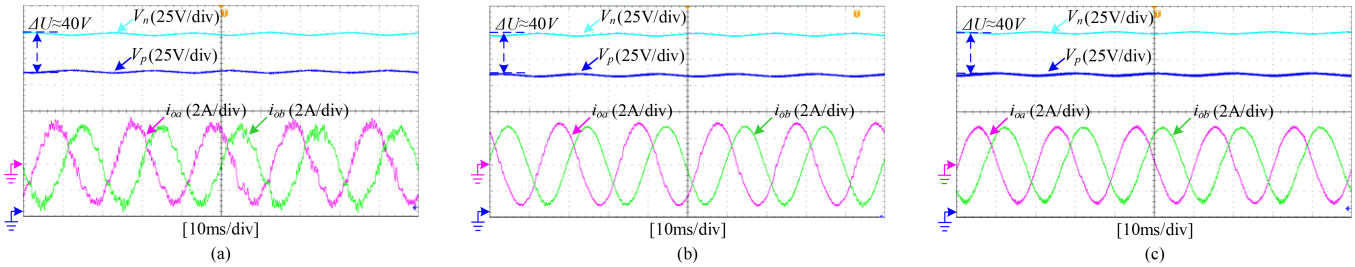

Fig. 14. Three-phase unbalance suppression experimental waveforms under Condition 5. (a) T-MPC. (b) T-SVPWM. (c) Proposed H-MPC.

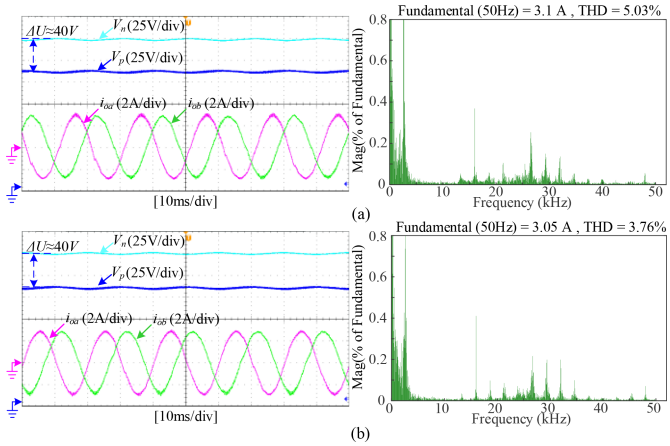

Fig. 15. Comparison of three-phase unbalance suppression. (a) H-MPC without vector reconstruction. (b) H-MPC with vector reconstruction.

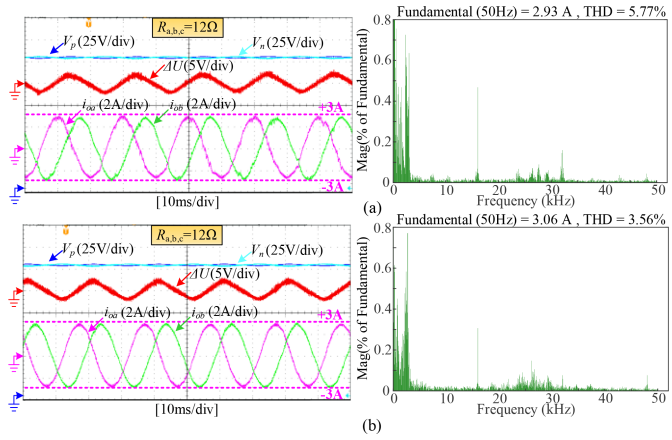

Fig. 16. Comparison experiments with weighting factor-based method under steady-state condition. (a) MPC with weighting factors. (b) Proposed H-MPC.

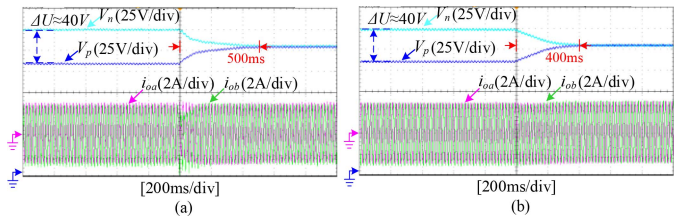

Fig. 17. Comparison experiments with weighting factor based method under dynamic condition. (a) MPC with weighting factors. (b) Proposed H-MPC.

H-MPC with and without vector reconfiguration. The experimental results are shown in Fig. 15. It can be seen that H-MPC with vector reconstruction demonstrates better output performance.

E. Comparison Experiments With Weighting Factor Based Method

To comprehensively evaluate the performance of the proposed NP voltage balancing method and the NP voltage balancing method based on weighting factors. Comparisons were made under steady-state and dynamic experimental conditions. For a fair comparison, the only difference between the two methods was the NP voltage balancing strategy, with the weight factor carefully tuned to $\lambda = 0.4$ for the conventional method through systematic trial and error.

Fig. 16 presents the comparative experimental waveform under steady-state conditions. It can be seen that both MPC methods can effectively achieve NP voltage balancing, and the NP voltage fluctuations under steady-state conditions are similar. However, due to the frequent selection of non-minimal-tracking-error sectors in the weighting factor-based MPC, the output ripple is large, and the THD under steady-state conditions is 5.77%. In contrast, the proposed H-MPC achieves superior performance with minimal impact on tracking accuracy while maintaining voltage regulation, yielding a substantially lower THD of 3.56%. Therefore, the H-MPC proposed in this article has better steady-state performance.

To further compare the dynamic performance of the two methods, a 40 V dc offset is initially added to the sampling signal. Subsequently, the offset is removed, and the recovery time for balance among the four algorithms is compared. The comparative experimental results are shown in Fig. 17. It can be seen that the recovery time of MPC with weighting factors is 500 ms, while the recovery time of the proposed H-MPC is 400 ms. Therefore, the proposed H-MPC has better dynamic performance. Furthermore, during this transient process, the weight factor-based MPC exhibits severe output waveform distortion, whereas the proposed H-MPC maintains nearly undisturbed waveform quality.

F. Model Parameter Mismatch Experiments

In practice, model parameter mismatch is inevitable due to various disturbances. In this section, the parameter sensitivity of MPC-based methods is evaluated by changing the filter inductor

TABLE IV
ANALYSIS OF PARAMETERS SENSITIVITY

ΔL/%	-50	-30	-10	0	+10	+30	+50
T-MPC/%	9.3	6.96	7.28	6.9	7.1	9	10.2
H-MPC/%	4.87	4.59	3.59	2.71	2.97	3.57	3.67
ΔR/%	-50	-30	-10	0	10	30	50
T-MPC/%	7.65	7.36	6.78	6.9	6.9	7.38	7.53
H-MPC/%	2.81	2.59	2.74	2.71	2.61	2.91	3.24

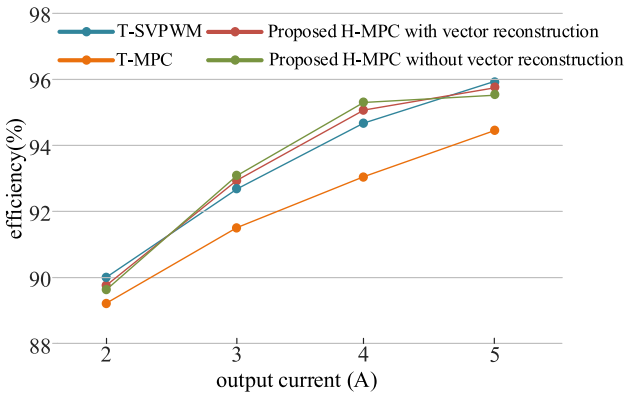

Fig. 18 Efficiency comparison experiments.

L_f and equivalent resistance R_L, where the change rate ΔL and ΔR are defined as

$$\begin{cases} \Delta L = \frac{\tilde{L}-L_r}{L_r} \times 100\% \\ \Delta R = \frac{\tilde{R}-R_r}{R_r} \times 100\% \end{cases} \tag{28}$$

where $\tilde{L}$ and $\tilde{R}$ are the filter inductor and equivalent resistance values used in the experiments, respectively. L_r and R_r are the real filter inductor and equivalent resistance values, respectively.

The experimental results of parameter sensitivity under Condition 6 are shown in Table IV. It can be observed that the H-MPC proposed in this article maintains a THD of less than 5% even with a 50% parameter mismatch. This demonstrates that the proposed method has better robustness compared to T-MPC.

G. Efficiency Comparison Experiments

System efficiency is an important indicator for evaluating MPC performance. Experiments were conducted across varying output currents. The system efficiency η is defined as

$$\eta = \frac{P_{\text{out}}}{P_{\text{in}}} \times 100\% \tag{29}$$

where P_{out} is the output power and P_{in} is the input power.

The experimental results under different output currents are shown in Fig. 18. It can be seen that as the output current increases, the system efficiency gradually improves. Compared with T-MPC, the proposed H-MPC has higher efficiency. In addition, regardless of whether there is voltage vector reconstruction, the efficiency of H-MPC is similar. These results confirm the superior efficiency of the proposed method.

TABLE V
EVALUATION OF DIFFERENT METHODS FOR ESTPIS

Methods	Com-plexity	Tuning Required	THD	Robust-ness	Weighting Factors
Traditional MPC	High	Required	High	Weak	With
SVPWM [19]	High	Required	Low	Strong	Without
MPC [17]	Low	Required	Low	Strong	Without
MPC [30]	High	Required	Low	Strong	With
Proposed H-MPC	Low	Required	Low	Strong	Without

H. Comparison of Different MPCs

Based on the experimental results, the performance of several advanced control methods for ESTPIs was summarized, as shown in Table V. In Table V, the "Complexity" term represents the execution time of different algorithms, the "Tuning Required" term indicates whether the tuning of parameters is required, and the "THD" term refers to the steady-state performance of different algorithms. In addition, the "Robustness" term refers to the sensitivity of different algorithms to parameter variations, while the "Weighting factors" term refers to whether the cost function includes weighting factors.

The results demonstrate that the proposed H-MPC has excellent performance and promising application prospects in ESTPIs.

V. CONCLUSION

A H-MPC is proposed for ESTPIs reconfigured by postfault 3P-3L VSIs. Comprehensive experiments have been carried out to verify the effectiveness of the method. Based on the above-mentioned analyses, the following conclusions can be drawn.

1) The proposed vector reconstruction method based on NP voltage enables H-MPC to achieve better steady-state performance and effectively suppresses the three-phase unbalance, with a THD of less than 4% at various reference currents. In addition, compared to T-MPC, H-MPC maintains a constant switching frequency.
2) The use of a PD controller eliminates the weighting factors in the cost function, allowing the reference current tracking to be decoupled from the NP voltage balance, thereby effectively balancing the NP voltage.
3) The proposed multistep optimization strategy significantly simplifies the computation, reducing the computation time by approximately 65.8% compared to the preoptimization period.

Therefore, the proposed H-MPC shows great promise for fault-tolerant technologies.

While the proposed H-MPC demonstrates promising fault-tolerant capabilities for ESTPIs reconfigured from postfault 3P-3L VSIs, its industrial adoption faces challenges, particularly in power range limitations—achieving only half the output power of the original topology. However, the eight-switch configuration

offers compelling cost advantages over redundant phase-leg solutions, suggesting potential as a complementary approach in applications where full redundancy is economically prohibitive.

Although experimentally validated with passive loads, the core control principles are extendable to bidirectional power flow applications, such as grid-tied converters and motor drives, by integrating additional control layers for power regulation or torque tracking, as well as to systems with nonlinear loads through appropriate harmonic compensation strategies. Future work will focus on expanding the operational power range through advanced modulation techniques and hybrid topologies, exploring integration with variable frequency drives to leverage its fast dynamic response and compact design, and investigating the critical transition phase during fault detection and system reconfiguration to ensure smooth control handover. These directions aim to bridge the gap between academic research and industrial practicality, addressing both performance and scalability concerns.

REFERENCES

[1] S. Kouro et al., "Recent advances and industrial applications of multilevel converters," *IEEE Trans. Ind. Electron.*, vol. 57, no. 8, pp. 2553–2580, Aug. 2010.

[2] R. Teichmann and S. Bernet, "A comparison of three-level converters versus two-level converters for low-voltage drives, traction, and utility applications," *IEEE Trans. Ind. Appl.*, vol. 41, no. 3, pp. 855–865, May/Jun. 2005.

[3] J. I. Leon, S. Vazquez, and L. G. Franquelo, "Multilevel converters: Control and modulation techniques for their operation and industrial applications," *Proc. IEEE*, vol. 105, no. 11, pp. 2066–2081, Nov. 2017.

[4] C. Yang et al., "Voltage difference residual-based open-circuit fault diagnosis approach for three-level converters in electric traction systems," *IEEE Trans. Power Electron.*, vol. 35, no. 3, pp. 3012–3028, Mar. 2020.

[5] Y. Song and B. Wang, "Survey on reliability of power electronic systems," *IEEE Trans. Power Electron.*, vol. 28, no. 1, pp. 591–604, Jan. 2013.

[6] U. M. Choi, J. S. Lee, F. Blaabjerg, and K. B. Lee, "Open-circuit fault diagnosis and fault-tolerant control for a grid-connected NPC inverter," *IEEE Trans. Power Electron.*, vol. 31, no. 10, pp. 7234–7247, Oct. 2016.

[7] B. Lu and S. K. Sharma, "A literature review of IGBT fault diagnostic and protection methods for power inverters," *IEEE Trans. Ind. Appl.*, vol. 45, no. 5, pp. 1770–1777, Sep./Oct. 2009.

[8] J. Chen, C. Zhang, X. Xing, and A. Chen, "A fault-tolerant control strategy for T-type three-level rectifier with neutral point voltage balance and loss reduction," *IEEE Trans. Power Electron.*, vol. 35, no. 7, pp. 7492–7505, Jul. 2020.

[9] S. Xu, Z. Sun, C. Yao, K. Liu, and G. Ma, "Open-switch fault-tolerant operation of T-type active neutral-point-clamped converter using level-shifted PWM," *IEEE Trans. Circuits Syst. II, Exp. Briefs*, vol. 68, no. 7, pp. 2598–2602, Jul. 2021.

[10] D. T. Do et al., "A redundant unit form of quasi-Z-source T-type inverter with fault-tolerant capability," in *Proc. 5th Int. Conf. Green Technol. Sustain. Develop.*, 2020, pp. 78–81.

[11] V. T. Tran, K. M. Nguyen, D. T. Do, and A. T. Nguyen-Phan, "Open-circuit fault-tolerant method for three-level T-type inverter with voltage gain enhancing," *IEEE Trans. Circuits Syst. II, Exp. Briefs*, vol. 71, no. 2, pp. 927–931, Feb. 2024.

[12] U. M. Choi, F. Blaabjerg, and K. B. Lee, "Reliability improvement of a T-type three-level inverter with fault-tolerant control strategy," *IEEE Trans. Power Electron.*, vol. 30, no. 5, pp. 2660–2673, May 2015.

[13] Y. Yao, W. Huang, R. Li, M. Yu, J. Liu, and J. Wu, "Active fault-tolerant control for three-level T-type converter with unbalanced neutral-point voltage modulation," *IEEE Trans. Power Electron.*, vol. 40, no. 10, pp. 15359–15370, Oct. 2025.

[14] U. M. Choi, K. B. Lee, and F. Blaabjerg, "Diagnosis and tolerant strategy of an open-switch fault for T-type three-level inverter systems," *IEEE Trans. Ind. Appl.*, vol. 50, no. 1, pp. 495–508, Jan./Feb. 2014.

[15] S. Li and L. Xu, "Strategies of fault tolerant operation for three-level PWM inverters," *IEEE Trans. Power Electron.*, vol. 21, no. 4, pp. 933–940, Jul. 2006.

[16] J. J. Park, T. J. Kim, and D. S. Hyun, "Study of neutral point potential variation for three-level NPC inverter under fault condition," in *Proc. 34th Annu. Conf. IEEE Ind. Electron.*, 2008, pp. 983–988.

[17] Z. Dou, Z. Chen, N. Wang, J. Song, N. Jin, and A. Zheng, "A voltage equalizing model predictive control strategy for 3-level T-type grid-tied fault-tolerant inverter," in *Proc. IEEE Int. Conf. Predictive Control Elect. Drives Power Electron.*, 2021, pp. 921–926.

[18] U. M. Choi, F. Blaabjerg, and K. B. Lee, "Reliability improvement of a T-type three-level inverter with fault-tolerant control strategy," *IEEE Trans. Power Electron.*, vol. 30, no. 5, pp. 2660–2673, May 2015.

[19] Q. Deng, X. Ge, C. Lin, D. Xie, B. Gou, and X. Feng, "An optimized SVPWM strategy for the postfault three-level NPC voltage source inverters," *IEEE Trans. Ind. Appl.*, vol. 57, no. 6, pp. 6182–6194, Nov./Dec. 2021.

[20] Y. C. Liu, X. Ge, X. Feng, and R. Ding, "Relationship between SVPWM and carrier-based PWM of eight-switch three-phase inverters," *Electron. Lett.*, vol. 51, no. 13, pp. 1018–1019, Jun. 2015.

[21] L. Yong-Chao, G. Xinglai, and T. Qidi, "Relationship between two different space-vector modulation methods of eight-switch three-phase inverters," in *Proc. IEEE 8th Int. Power Electron. Motion Control Conf.*, 2016, pp. 3206–3210.

[22] Q. Yan et al., "Optimization of the symmetrical SVPWM for three-level T-type inverters with unbalanced and oscillated neutral-point voltages," *IEEE Trans. Ind. Electron.*, vol. 71, no. 4, pp. 4026–4037, Apr. 2024.

[23] S. Vazquez, J. Rodriguez, M. Rivera, L. G. Franquelo, and M. Norambuena, "Model predictive control for power converters and drives: Advances and trends," *IEEE Trans. Ind. Electron.*, vol. 64, no. 2, pp. 935–947, Feb. 2017.

[24] J. Rodriguez et al., "State of the art of finite control set model predictive control in power electronics," *IEEE Trans. Ind. Inform.*, vol. 9, no. 2, pp. 1003–1016, May 2013.

[25] F. Donoso, A. Mora, R. Cárdenas, A. Angulo, D. Sáez, and M. Rivera, "Finite-set model-predictive control strategies for a 3L-NPC inverter operating with fixed switching frequency," *IEEE Trans. Ind. Electron.*, vol. 65, no. 5, pp. 3954–3965, May 2018.

[26] Y. Yang, H. Wen, and D. Li, "A fast and fixed switching frequency model predictive control with delay compensation for three-phase inverters," *IEEE Access*, vol. 5, pp. 17904–17913, 2017.

[27] N. Jin, M. Chen, L. Guo, Y. Li, and Y. Chen, "Double-vector model-free predictive control method for voltage source inverter with visualization analysis," *IEEE Trans. Ind. Electron.*, vol. 69, no. 10, pp. 10066–10078, Oct. 2022.

[28] Y. Yang, H. Wen, M. Fan, M. Xie, and R. Chen, "Fast finite-switching-state model predictive control method without weighting factors for T-type three-level three-phase inverters," *IEEE Trans. Ind. Inform.*, vol. 15, no. 3, pp. 1298–1310, Mar. 2019.

[29] B. Long, T. Cao, D. Sheng, J. Rodriguez, J. M. Guerrero, and K. T. Chong, "Sequential model predictive fault-tolerance control for T-type three-level grid-connected converters with LCL filters," *IEEE Trans. Ind. Electron.*, vol. 69, no. 9, pp. 9039–9051, Sep. 2022.

[30] C. Xiang, Z. Ouyang, X. Zhang, H. H. C. Iu, and S. Cheng, "An improved predictive current control of eight switch three-level post-fault inverter with common mode voltage reduction," *IEEE Trans. Circuits Syst. I, Reg. Papers*, vol. 69, no. 9, pp. 3861–3872, Sep. 2022.

[31] C. Xiang, X. Zhang, H. H. C. Iu, L. Zhang, and S. Cheng, "Duty VV-MPTC for post-fault eight switch three-phase inverter fed induction motor drives with reduced neutral point voltage fluctuation," *IEEE Trans. Power Electron.*, vol. 36, no. 10, pp. 11691–11700, Oct. 2021.

Yong Yang (Senior Member, IEEE) received the B.S. degree in automation from Xiangtan University, Xiangtan, China, in 2003, the M.S. degree in electrical engineering from Guizhou University, Guiyang, China, in 2006, and the Ph.D. degree in electrical engineering from Shanghai University, Shanghai, China, in 2010.

He is currently a Full Professor with the School of Rail Transportation, Soochow University. From Dec. 2017 to Dec. 2018, he was a Visiting Scholar with Center for High Performance Power Electronics, The Ohio State University, Columbus, USA. He has authored or coauthored more than 80 IEEE Transactions papers and is the holder of more than 60 patents in these areas. His current research interests include model predictive control in power electronic converters, distributed energy resource interfacing, and high-performance motor drive control.

Youcheng Wang received the B.S. degree in electrical engineering from Soochow University, Suzhou, China, in 2022, and the M.S. degree in transportation engineering from Soochow University, Suzhou, China, in 2025.

His research interest includes model predictive control in power electronic converters.

Rong Chen was born in Jiangsu, China, in 1983. She received the B.S. degree in communication engineering, the M.S. degree in communication and information system, and the Ph.D. degree in signal and information processing from Soochow University, Suzhou, China, in 2006, 2009, and 2013, respectively.

She is currently an Associate Professor with the School of Rail Transportation, Soochow University. Her research interests include signal processing and synchronous phasor measuring.

Jiefeng Hu (Senior Member, IEEE) received the Ph.D. degree in electrical engineering from the University of Technology Sydney, Ultimo, NSW, Australia, in 2013.

He participated in the research of minigrids in Commonwealth Scientific and Industrial Research Organization, Newcastle, Australia. He was an Assistant Professor with The Hong Kong Polytechnic University, Hong Kong. He is currently an Associate Professor and a Program Coordinator of Electrical Engineering with Federation University Australia, Ballarat, VIC, Australia, where he is also the Stream Leader of Centre for New Energy Transition Research. His research interests include power electronics, renewable energy, and smart microgrids.

Dr. Hu is an Associate Editor for *IET Renewable Power Generation*, an Editor for IEEE Transactions on Energy Conversion, an Associate Editor for IEEE ACCESS, and was a Guest Editor for IEEE TRANSACTIONS ON INDUSTRIAL ELECTRONICS for a Special Issue "Applications of Predictive Control in Microgrids."

Huiqing Wen (Senior Member, IEEE) received the B.S. and M.S. degrees in electrical engineering from Zhejiang University, Hangzhou, China, in 2002 and 2006, respectively, and the Ph.D. degree in electrical engineering from the Chinese Academy of Sciences, Beijing, China, in 2009.

From 2009 to 2010, he was an Electrical Engineer working in the Research and Development Center, GE (China) Co., Ltd., Shanghai, China. From 2010 to 2011, he was an Engineer at the China Coal Research Institute, Beijing, China. From 2011 to 2012, he was a Postdoctoral Fellow with the Masdar Institute of Science and Technology, Abu Dhabi, United Arab Emirates. He is presently working as a Full Professor with the Xi'an Jiaotong-Liverpool University, Suzhou, China. His current research interests include bidirectional dc–dc converters, power electronics in flexible ac transmission applications, electrical vehicles, high-power, and three-level electrical driving systems.

Yiwang Wang (Member, IEEE) received the B.S. degree in electrical engineering and automation from the Kunming University of Science and Technology, Kunming, China, in 2005, and the Ph.D. degree in electrical engineering from Shanghai Jiao Tong University, Shanghai, China, in 2020.

He is currently a Professor with the Collaborative Innovation Center of Smart Energy Equipment and Power Conversion, Suzhou Polytechnic University, Suzhou, China. He is also a Director of Suzhou Key Laboratory of Smart Energy Technology and Jiangsu Engineering Research Center for PV Generation. His research interests include power electronics intelligent control, and the applications of power electronics and renewable energy.

Hui Yang (Senior Member, IEEE) received the B.Eng. degree from Dalian University of Technology, Dalian, China, in 2011, and the Ph.D. degree from Southeast University, Nanjing, China, in 2016, respectively, both in electrical engineering.

From 2014 to 2015, he was supported by the China Scholarship Council through a one-year joint Ph.D. studentship with The University of Sheffield, Sheffield, U.K. From 2019 to 2020, he was a Postdoctoral Fellow with the School of Electrical Engineering, The Hong Kong Polytechnic University. From 2016 to 2024, he was with Southeast University, China, and he is currently a Full Professor with the College of Automation Engineering, Nanjing University of Aeronautics and Astronautics. He has authored or coauthored more than 120 IEEE Transactions papers and is the holder of more than 40 patents in these areas. His research interests include novel permanent-magnet machines and drives with particular reference to variable-flux machines for electric vehicles, robotics, and renewable energy applications.

Dr. Yang serves as Associate Editor of IEEE TRANSACTIONS ON INDUSTRIAL ELECTRONICS, IEEE TRANSACTIONS ON ENERGY CONVERSION, and Editor of WEVJ. He was Organizing Committee Chair of iSPEC 2021 and CIEEC 2022.

Jose Rodriguez (Life Fellow, IEEE) received the Engineering degree in electrical engineering from the Universidad Tecnica Federico Santa Maria, Valparaiso, Chile, in 1977, and the Dr.-Ing. degree in electrical engineering from the University of Erlangen, Erlangen, Germany, in 1985.

He has been with the Department of Electronics Engineering, Universidad Tecnica Federico Santa Maria, since 1977, where he was Full Professor and President. Since 2015 to 2019, he was the President with Universidad Andres Bello in Santiago, Chile. Since 2022, he is President with Universidad San Sebastian, Santiago, Chile. He has coauthored two books, several book chapters and more than 700 journal and conference papers. His main research interests include multilevel inverters, new converter topologies, control of power converters, and adjustable-speed drives.

Dr. Rodriguez was the recipient of number of best paper awards from journals of the IEEE. He is Member of the Chilean Academy of Engineering, recipient of the National Award of Applied Sciences and Technology from the government of Chile, in 2014, and the recipient of Eugene Mittelmann Award from the Industrial Electronics Society of the IEEE, in 2015. In years 2014 to 2021, he was included in the list of Highly Cited Researchers published by Web of Science.